Chemical Science

ROYAL SOCIETY OF CHEMISTRY

EDGE ARTICLE

View Article Online
View Journal | View Issue

Cite this: *Chem. Sci.*, 2025, **16**, 5089

All publication charges for this article have been paid for by the Royal Society of Chemistry

Donor modulation brings all-in-one phototheranostics for NIR-II imaging-guided type-I photodynamic/photothermal synergistic cancer therapy†

Yuxin Ren, Xinyi Zhang, Ling Li, Qiong Yuan, Benkai Bao, Meiqi Li and Yanli Tang *

Type-I photodynamic (PDT) and photothermal (PTT) synergistic therapy guided by fluorescence imaging in the near-infrared region II (NIR-II) is crucial for cancer diagnosis and treatment. Phototheranostics provide a promising system for efficient imaging-guided phototherapy, combining diagnostics with therapeutics within a single photosensitizer and avoiding the complexity of composition and low reproducibility of combination methods. Herein, we design and synthesize an all-in-one phototheranostic agent OTAB by modifying aza-BODIPY with a methoxy group substituted triphenylamine moiety, followed by the formation of nanoparticle OTAB@cRGD NPs *via* self-assembly with DSPE-PEG_{2000}-cRGD. Structurally, the methoxy-modified triphenylamine moiety as a strong electron donor can reduce the singlet–triplet energy gap (ΔE_{S1-T1}) by creating a strong intramolecular charge transfer state, thereby accelerating the intersystem crossing process and thus preferentially generating $O_2^{\bullet-}$ *via* electron transfer. A single 808 nm laser can trigger its NIR-II imaging and excellent type-I photodynamic and photothermal therapy. Furthermore, OTAB@cRGD NPs with high photostability, colloid stability and biocompatibility can actively target tumor tissue *via* intravenous injection. Thus, tumor localization and imaging diagnosis are successfully realized. The PDT/PTT synergistic therapy brings efficient tumor inhibition and ablation both *in vitro* and *in vivo*. Therefore, this work provides a new strategy to construct an all-in-one multifunctional probe for the integration of NIR-II diagnosis and treatment.

Received 24th December 2024
Accepted 28th January 2025

DOI: 10.1039/d4sc08685f

rsc.li/chemical-science

Introduction

Cancer has become a major disease that seriously threatens human health and social development.[1,2] The integration of diagnosis and therapy could provide a vital strategy for cancer treatment. At present, phototherapy represents a promising treatment that uses light to selectively ablate tumor cells and reduce their aggressiveness to a minimum. It is classified into photothermal therapy (PTT) and photodynamic therapy (PDT).[3] The heating effect of PTT enhances the delivery of PDT agents to the intracellular environment and increases the oxygen concentration in tumor tissue by improving local blood flow, thereby improving the efficacy of PDT. Meanwhile, reactive oxygen species (ROS) generated by PDT block heat shock proteins, thus inhibiting the protective effect of proteins in cancer cells during PTT and making the cells more sensitive to heat. Therefore, the synergistic effect of PTT and PDT can achieve a therapeutic effect of "1 + 1 > 2".[4,5] Additionally, NIR-II optical diagnostic agents are considered promising tools for preoperative cancer detection because fluorescence imaging in the second near-infrared window (NIR-II, 1000–1700 nm) has a deeper penetration depth and higher resolution ratio than visible light and the NIR-I window.[6–9] In order to achieve simultaneous NIR-II diagnostic and PDT/PTT synergistic therapeutic purposes, a common strategy is to combine multiple components with individual advantages into a nanoplatform.[10,11] However, this approach suffers from the drawbacks of complexity of composition,[12] different wavelengths of laser irradiation,[13] and low reproducibility.

Recently, phototheranostics have provided a promising system for efficient imaging-guided phototherapy for cancer, combining diagnostics with therapeutics within a single photosensitizer (PS). Some single-component all-in-one phototheranostics, including inorganic and organic phototheranostics, have been reported for imaging and therapy.[14–17] However, inorganic phototheranostics have limited clinical applications due to their poor biocompatibility. Organic phototheranostics have gained more and more attention due to their good biocompatibility and ease of modification.[18] In particular, aza-boron-dipyrromethene (Aza-BODIPY) derivatives

Key Laboratory of Analytical Chemistry for Life Science of Shaanxi Province, Key Laboratory of Applied Surface and Colloid Chemistry, Ministry of Education, School of Chemistry and Chemical Engineering, Shaanxi Normal University, Xi'an, Shaanxi Province 710119, P. R. China. E-mail: yltang@snnu.edu.cn

† Electronic supplementary information (ESI) available. See DOI: https://doi.org/10.1039/d4sc08685f

are promising agents for phototheranostics due to their long-wavelength absorption and emission, high photostability and high molar extinction coefficients, and have been reported in *in vivo* imaging and treatments.[19–21] However, even though phototheranostics possess NIR-II fluorescence, most of them, including aza-BODIPY-based small molecules, tend to produce singlet oxygen ($^1O_2$) through the oxygen-consuming type-II energy transfer process, leading to an insufficient tumor-killing effect in the low-oxygen tumor microenvironment.[22] To alleviate the dependence on oxygen, type-I photosensitizers are a better choice for PDT, as they can use e^-/H^+ transfer to generate cytotoxic free radicals (*e.g.*, $O_2^{\bullet-}$ and ·OH). The design of type-I photosensitizers is a considerable challenge because the energy transfer process in type-II is much faster than the electron transfer process in type-I.[23–25] Therefore, it is urgent and challenging to develop new strategies for designing all-in-one phototheranostics with NIR-II fluorescence and type-I PDT/PTT therapy.[26–29]

Herein, we report a new strategy to design all-in-one NIR-II phototheranostics for the diagnosis and therapy of cancers based on aza-BODIPY. Considering the electron-deficient nature of the aza-BODIPY core structure, we attempted to modify the aza-BODIPY with a methoxy group substituted triphenylamine moiety to synthesize the OTAB molecule (Scheme 1). There are three advantages to this design: (1) benefiting from the strong electron-donor effect of the triphenylamine moiety, OTAB possesses excellent NIR-II emission, facilitating imaging and treatment of deep tumors; (2) methoxyl groups on the triphenylamine could promote triplet state sensitization and accelerate the intersystem crossing (ISC) process of the excited state, making the resulting T1 energy level insufficient to sensitize $^3O_2$ to $^1O_2$ *via* the type II pathway;[30,31] (3) the free rotation of the benzene ring can also promote photothermal conversion, producing PDT/PTT synergistic treatment.[32] To further enhance the tumor targeting ability, OTAB was prepared as nanoparticles OTAB@cRGD NPs using liposomes (DSPE-

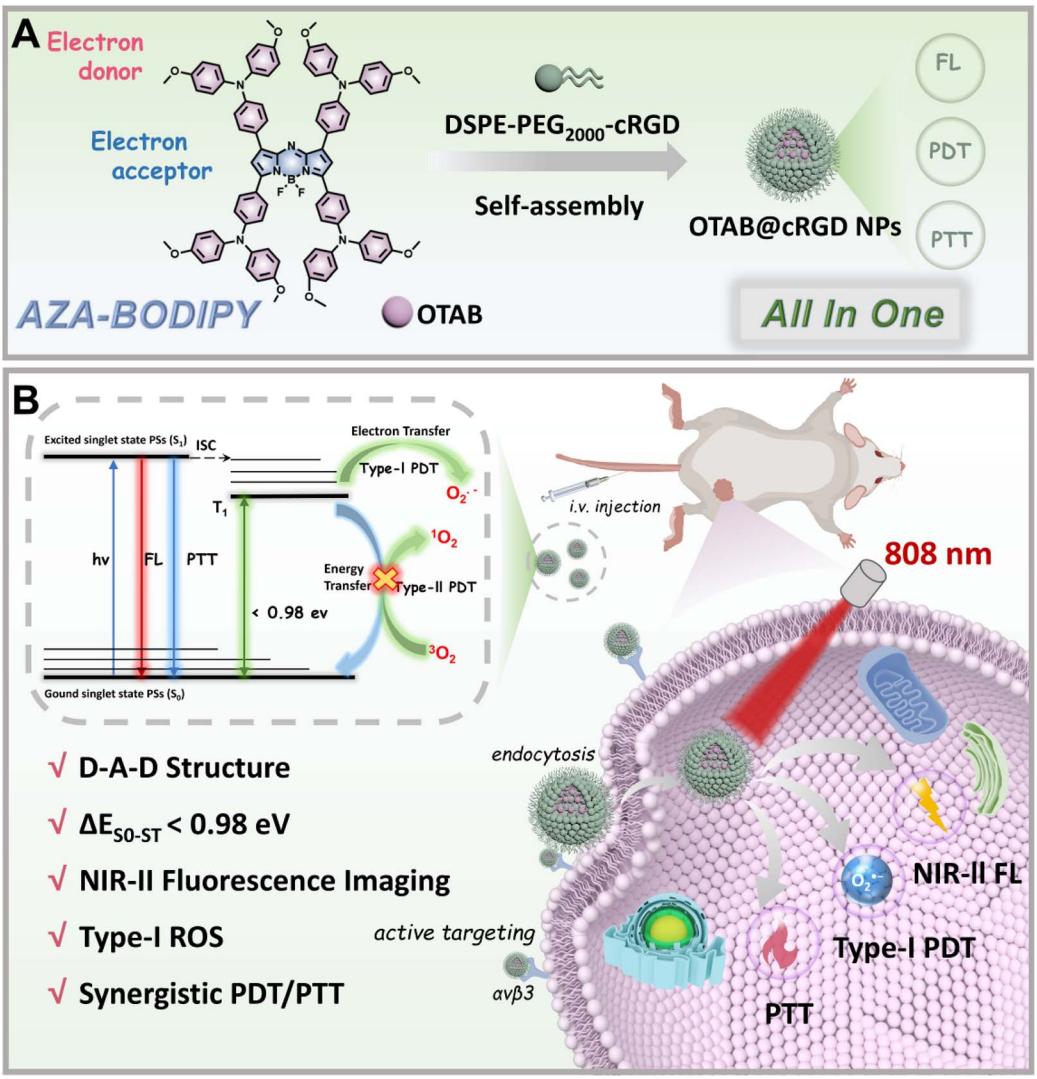

Scheme 1 (A) Preparation of OTAB@cRGD NPs *via* a nanoprecipitation method. (B) Illustration of OTAB@cRGD NPs with NIR-II fluorescence for synergistic PDT/PTT cancer therapy.

PEG_{2000}-cRGD) as carriers. *In vitro* and *in vivo* experiments demonstrated that OTAB@cRGD NPs could profoundly inhibit the proliferation of breast cancer cells and tumor growth by synergistic type-I PDT/PTT phototherapy guided by NIR-II fluorescence imaging.

Results and discussion

Design and synthesis of OTAB

To design all-in-one phototheranostics, the methoxy-modified triphenylamine moiety as a donor was covalently linked to the aza-BODIPY core structure *via* the classical synthetic route of O'Shea.[33] Notably, the methoxy-modified triphenylamine moiety can also act as a molecular rotor, creating a twisted, propeller-like structure, which prevents fluorescence bursting in the aggregated state by restricting the Π–Π stacking of the molecules.[34] At the same time, it can act as an extender of the molecular conjugation length, resulting in longer fluorescence emission. Additionally, the methoxy group can promote triple state sensitization and accelerate the ISC process in the excited state, and the free rotation of the benzene ring can also promote photothermal conversion, thus achieving a balance between PDT and PTT. The synthetic route of OTAB is shown in Fig. 1A. The structure of the target product OTAB and its intermediates were identified through the ^{1}H NMR, ^{13}C NMR, ^{19}F NMR and MALDI-TOF-MS (Fig. S1–S19†). As shown in Fig. S16†, the signals around 3.81 and 3.79 ppm are associated with the methoxy group in OTAB, while the peaks between 6.81–7.95 ppm are assigned to the signal of triphenylamine and aza-BODIPY core. In addition, the MALDI-TOF-MS spectrum of OTAB showed a peak at m/z = 1405.3 (Fig. S19†), corresponding to the theoretical value of 1405.57. All of the above characterizations demonstrated that OTAB has been successfully synthesized.

Theoretical calculations for OTAB

To validate our design strategy, the electronic structure was first evaluated using density functional theory (DFT) calculations. As

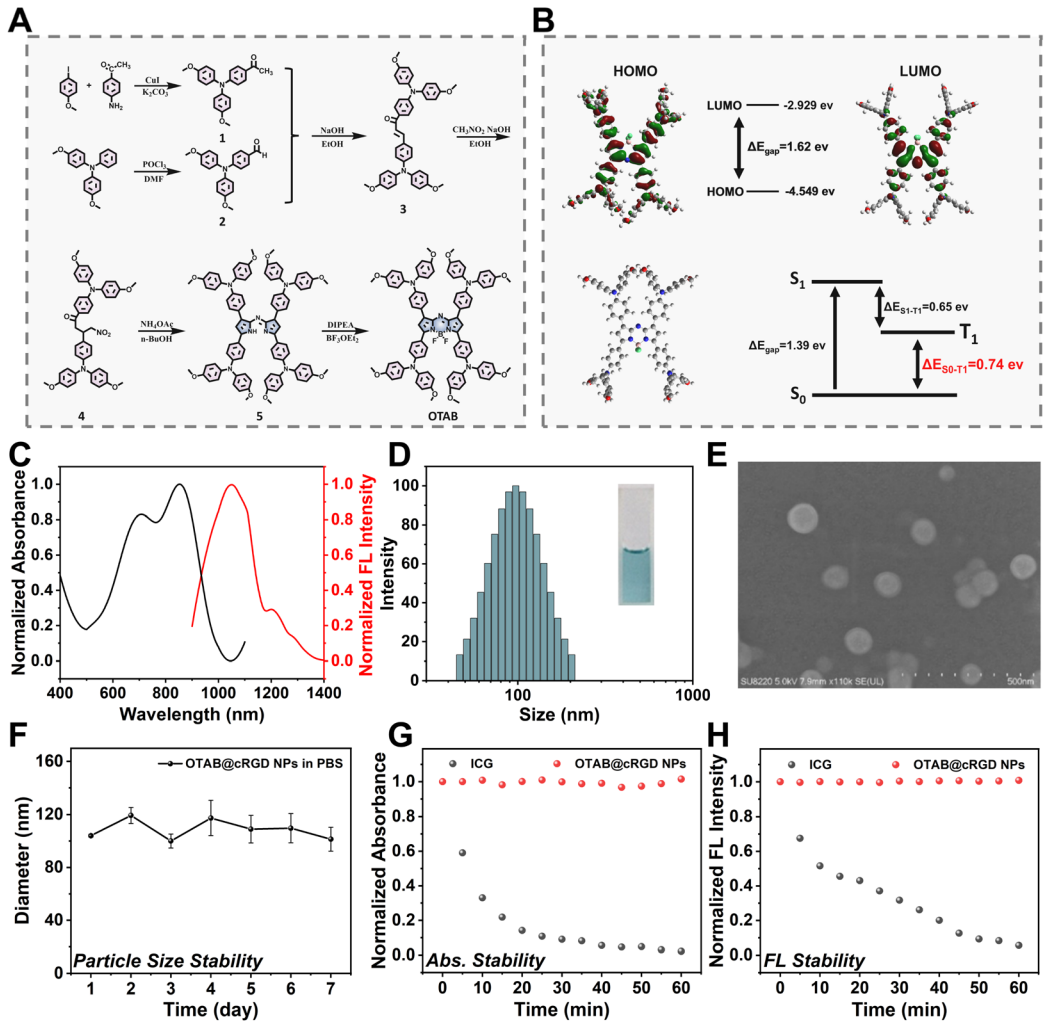

Fig. 1 (A) The synthesis route of OTAB. (B) Calculated HOMO and LUMO energy levels, dihedral angles and the energy level difference between the singlet and triplet states for OTAB. (C) Normalized absorption and emission spectra of OTAB. (D) DLS data of OTAB@cRGD NPs with corresponding photographs (inset). (E) The SEM image of OTAB@cRGD NPs. (F) The hydrodynamic diameter of OTAB@cRGD NPs in PBS for different periods. (G) The normalized absorbance and (H) the normalized FL intensity of ICG and OTAB@cRGD NPs solutions upon constant laser exposure for 60 min (808 nm, 1.0 W cm^{-2}).

shown in Fig. 1B, the highest occupied molecular orbital (HOMO) wave function was well out of domain along the entire molecular backbone, and the energy gap (ΔE_{gap}) between the HOMO and the lowest unoccupied molecular orbital (LUMO) of OTAB was 1.62 eV, whereas the LUMO wave function was mainly localized in the aza-BODIPY backbone of the OTAB molecule, suggesting that there was an effective intramolecular charge transfer within the OTAB molecule. The dihedral angle of the pyrrole moiety (the aza-BODIPY plane) of OTAB to the benzene ring was calculated to be 22.6°, indicating that with the introduction of the helically twisted triphenylamine moiety, OTAB tended to form the stronger twisted conformation along the main chain. Notably, the calculated value of the energy gap between the ground state and triplet state (ΔE_{S0-T1}) was 0.74 eV, which was smaller than the oxygen sensitization threshold of 0.98 eV and was facilitated by the methoxy groups. This result suggested that the electron transfer process between the excited OTAB and the surrounding substrates was favored, preferring to perform type-I rather than type-II PDT.[35,36]

Photophysical properties of OTAB

After the target compound was synthesized, the fundamental photophysical properties of the multifunctional molecule OTAB were assessed in the molecular state. Firstly, the absorption and emission spectra of OTAB were measured in DMSO. As shown in Fig. 1C, OTAB has two absorption peaks at 698/858 nm, with maximum fluorescence emission at 1050 nm and the stokes shift up to 192 nm. Then, absorption spectra were recorded for OTAB in different concentrations and different solvents (Fig. S20†). With the increase in concentration, the absorbance also increased in direct proportion, which showed that the absorbance was concentration-dependent. As the solvent polarity increased, the maximum absorption wavelength of OTAB underwent a small redshift. The relative fluorescence quantum yield (QY) of OTAB was 0.38% in comparison to indocyanine green (ICG) (Fig. S21†), which was higher than the NIR-II aza-BODIPY of the similar type (0.088%, 0.064%).[37] The superior absorption and emission wavelengths of the OTAB probe suggested that it has a high potential for use in NIR-II fluorescence imaging-guided PDT/PTT therapy.

Preparation and characterization of OTAB@cRGD NPs

Considering that OTAB was highly hydrophobic, we used liposomes DSPE-PEG_{2000}-cRGD containing the target peptide cyclic arginine–glycine–aspartic acid (cRGD) as nanocarriers to encapsulate OTAB to form OTAB@cRGD NPs *via* nanoprecipitation,[38] which can improve the water solubility and enhance the biocompatibility and tumor targeting. As shown in Fig. 1D, dynamic light scattering (DLS) measurements showed that the hydration kinetic diameter of the OTAB@cRGD NPs was 102 nm with a polymer dispersity index (PDI) of 0.204. The SEM images showed that the nanoparticles were spherical and uniform in size (Fig. 1E). In addition, the particle size of OTAB@cRGD NPs did not change significantly in phosphate-buffered saline (PBS) after several days, indicating that the NPs had good colloid stability (Fig. 1F). The OTAB@cRGD NPs also exhibited a NIR absorption peak (Fig. S22A†) near 860 nm, which was slightly red-shifted compared with the OTAB molecule alone. As shown in Fig. S22B†, when exposed to an 808 nm laser, OTAB@cRGD NPs exhibited a fluorescence emission peak at 1069 nm, which lays the groundwork for the subsequent application in the NIR-II region. As shown in Fig. 1G and H, the normalized absorbance and the normalized fluorescence intensity of OTAB@cRGD NPs were almost unchanged even after 60 min irradiation compared with ICG, proving the excellent photostability of OTAB@cRGD NPs. OTAB@cRGD NPs had a zeta potential of -31.89 ± 3.5 mV, and the negative surface charge of the liposomes would significantly contribute to the long blood circulation and minimal reticuloendothelial system clearance.[39]

Photodynamic, photothermal and fluorescence properties assessment of OTAB@cRGD NPs

To investigate the photodynamic therapeutic performance of OTAB@cRGD NPs under 808 nm laser irradiation (1.0 W cm^{-2}), 2′,7′-dichlorofluorescein diacetate (DCFH-DA) was used as an index to evaluate total ROS generation. As shown in Fig. 2A and S23,† the fluorescence signal of DCFH alone remained almost unchanged under 808 nm irradiation for 6 min. However, the fluorescence intensity of DCFH mixed with OTAB@cRGD NPs continued to increase, reaching more than 35-fold under the same conditions, showing an amazing photodynamic performance. To determine the type of ROS, dihydroethidium (DHE) and dihydrorhodamine 123 (DHR 123) were used to detect the superoxide anion ($O_2^{\bullet-}$), and 9,10-anthracenediyl-bis(methylene) dimalonic acid (ABDA) was used to detect $^1O_2$. In the presence of OTAB@cRGD NPs, the absorbance of ABDA remained unchanged after 6 min of irradiation, indicating that the prepared NPs did not produce $^1O_2$ *via* the type-II pathway (Fig. 2B). Under 808 nm laser irradiation, the fluorescence intensity of DHE and DHR123 with OTAB@cRGD NPs resulted in a dramatic increase within 6 min, reflecting its rapid $O_2^{\bullet-}$ generation efficiency (Fig. 2C and D). In order to further verify the free radical species, the electron paramagnetic resonance (EPR) method was used to detect the generation of superoxide anion radicals. With 5,5-dimethyl-1-pyrroline *N*-oxide (DMPO) as the spin trapping agent and methanol solution as the ambient system, OTAB@cRGD NPs exhibited higher characteristic EPR signals under light conditions than under dark conditions, which indicated that OTAB@cRGD NPs can generate $O_2^{\bullet-}$ (Fig. 2E). DMPO was used as the self-selected capture agent and the aqueous solution was used as the ambient system for the detection of ·OH. The results showed that no characteristic peaks of hydroxyl radicals were generated in OTAB@cRGD NPs under laser irradiation, indicating that no ·OH radicals were produced (Fig. S24†). When 2,2,6,6-tetramethyl-4-piperidone hydrochloride (TEMP) was used as a spin-trapping agent for the detection of singlet oxygen signals, no significant EPR signals were generated compared with TEMP alone, further confirming that singlet oxygen was not generated (Fig. 2F). The above results suggested that OTAB@cRGD NPs can be used as efficient type-I photosensitizers to generate $O_2^{\bullet-}$ for PDT.

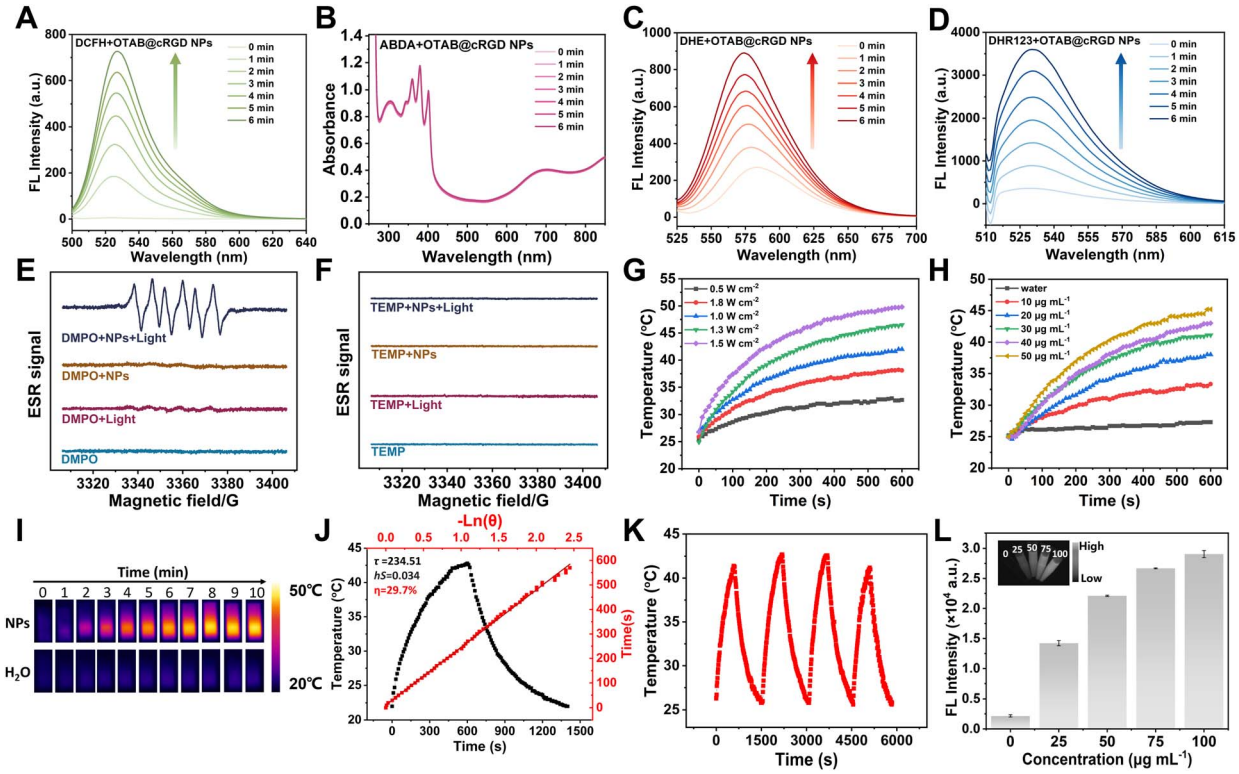

Fig. 2 (A) Fluorescence intensity of DCFH-DA in the presence of OTAB@cRGD NPs under illumination. (B) Absorbance changes of the ABDA probe in the presence of OTAB@cRGD NPs under illumination. Fluorescence intensity of (C) DHE and (D) DHR123 in the presence of OTAB@cRGD NPs under illumination. (E) ESR spectra of $O_2^{\bullet-}$ generated by the OTAB@cRGD NPs under illumination. (F) ESR spectra of $^1O_2$ generated by the OTAB@cRGD NPs under illumination. Temperature variation of OTAB@cRGD NPs with (G) different laser power densities ([OTAB@cRGD NPs] = 25 μg mL^{-1}) and (H) different concentrations (808 nm, 1.0 W cm^{-2}). (I) IR thermal images of the heating process of various concentrations of OTAB@cRGD NPs. (J) Calculation of PCE of OTAB@cRGD NPs. (K) Thermostability of OTAB@cRGD NPs in water exposed to an 808 nm laser for four cycles. (L) The mean fluorescence intensity of OTAB@cRGD NPs with various concentrations in PBS (808 nm laser, 0.3 W cm^{-2}, 1000 nm long-pass filter). The inset shows their NIR-II fluorescent images.

Due to the presence of flexible D–A chains in OTAB, it is speculated that OTAB@cRGD NPs may generate a large amount of thermal energy. As shown in Fig. 2G and H, the temperature rise curves of OTAB@cRGD NPs at different laser powers and different concentrations were recorded. The temperature rise was directly correlated with the increase in laser power density and NPs concentration. In particular, the temperature of OTAB@cRGD NPs (50 μg mL^{-1}) showed an increase from 25.0 to 45.2 °C (ΔT = 20.2 °C) under 808 nm laser irradiation (1.0 W cm^{-2}), which was sufficient to induce cancer cell death. In addition, thermal infrared images of OTAB@cRGD NPs were obtained under 808 nm laser irradiation for 10 min (Fig. 2I), which further confirmed the good photothermal properties of the nanoparticles. To quantitatively measure the ability of OTAB@cRGD NPs to convert absorbed light energy into heat energy, the photothermal conversion efficiency (PCE) of OTAB@cRGD NPs was calculated to be 29.7% (Fig. 2J), which is presented in detail in the ESI.† In addition, the thermal stability of OTAB@cRGD NPs was evaluated. As shown in Fig. 2K, the change in the heating-up curve of OTAB@cRGD NPs in an aqueous solution was negligible even after four heating–cooling cycles. These results demonstrated the excellent photothermal conversion performance and thermal stability of OTAB@cRGD NPs, making them suitable for potential photothermal applications. Furthermore, under 808 nm laser irradiation, *in vitro* imaging showed that the NIR-II fluorescence signal was gradually enhanced with the increase in the concentration of OTAB@cRGD NPs in the aqueous medium and the fluorescence intensity was positively correlated with the concentration of OTAB@cRGD NPs (Fig. 2L). The above experimental results indicate that OTAB@cRGD NPs can be used for NIR-II fluorescence imaging-guided type-I PDT/PTT synergistic therapy. A comparison of OTAB and OTAB@cRGD NPs with the recently reported NIR-II aza-BODIPY photosensitizers is shown in Table S1†. Our synthesized OTAB and prepared OTAB@cRGD NPs have a longer fluorescence emission wavelength and are the first to be used as all-in-one phototheranostics with NIR-II fluorescence and type-I PDT/PTT therapy.

Cell uptake and phototherapy *in vitro*

After confirming the excellent type-I PDT/PTT properties of OTAB@cRGD NPs, *in vitro* phototherapy studies of OTAB@cRGD NPs were carried out. In order to further verify the targeting effect of OTAB@cRGD NPs on tumor cells, OTAB was encapsulated with DSPE-PEG$_{2000}$ to form OTAB NPs as a control.

First, the methylthiazolyldiphenyl-tetrazolium bromide (MTT) method was used to detect the cytotoxicity of OTAB@cRGD NPs and OTAB NPs on HUVEC cells. When the concentration of OTAB@cRGD NPs even reached 50 μg mL^{-1}, the survival rate of cells still was more than 80%, which indicated that the nanoparticles had great biocompatibility (Fig. 3A). Next, the tumor cell viabilities were detected after 4T1 cells (mouse breast cancer cell line) and MDA-MB-231 cells (human breast cancer cell line) were incubated with the NPs. As shown in Fig. 3B and C, when the concentrations reached 30 μg mL^{-1}, more than 80% of the cells were alive without illumination, indicating that the NPs were not significantly toxic under dark conditions. Additionally, at a concentration of 25 μg mL^{-1}, the survival rates of both 4T1 and MDA-MB-231 cells in the presence of OTAB@cRGD NPs were lower than that in the presence of OTAB NPs under irradiation, confirming that targeted nanoparticles can enhance the killing ability of breast cancer cells. Furthermore, live/dead staining assays of 4T1 cells by calcein acetoxymethyl ester (calcein AM, green for live cells) and pyridinium iodide (PI, red for dead cells) were performed. As shown in Fig. 3D, bright green fluorescence was detected in unirradiated 4T1 cells, and the red fluorescence signal was negligible,

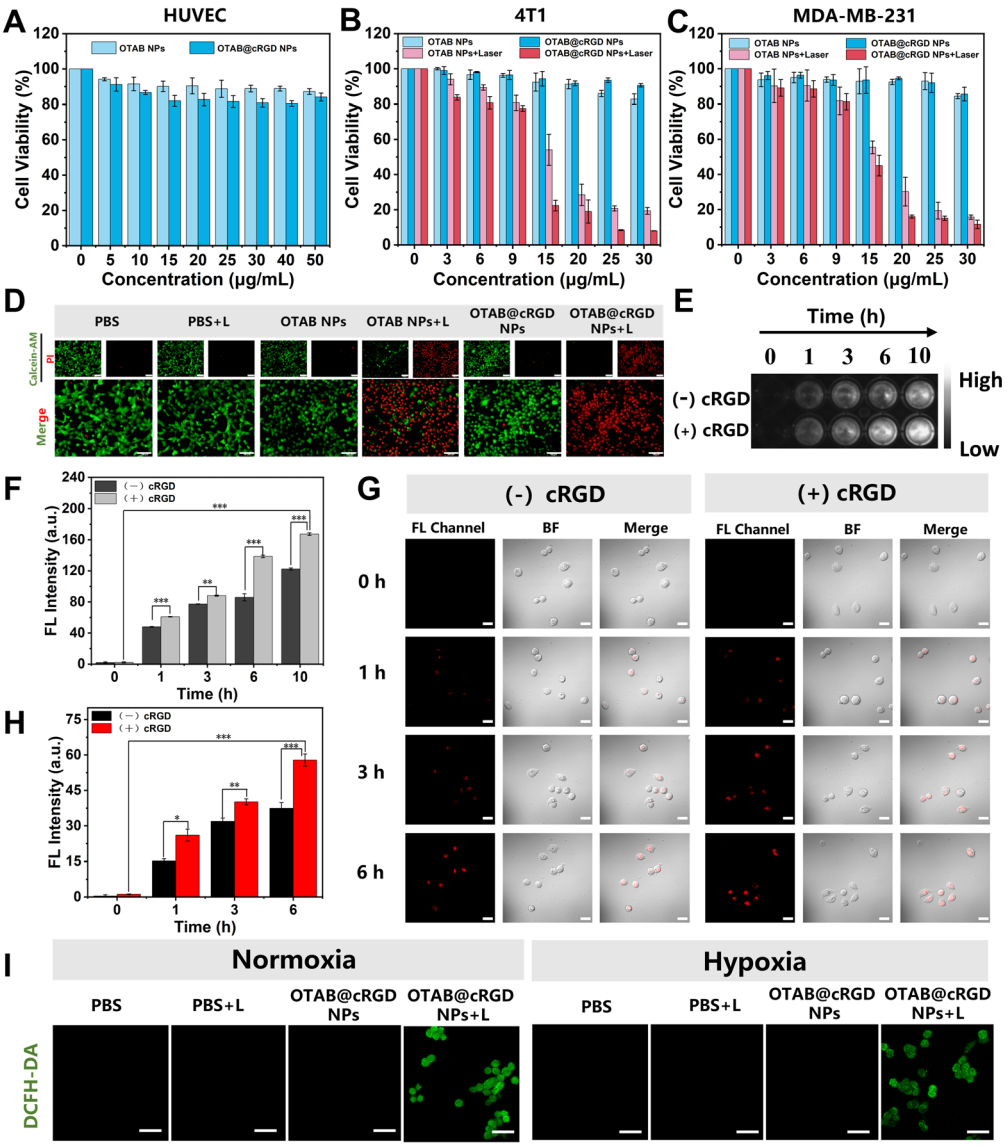

Fig. 3 Cell viability of (A) HUVEC cells, (B) 4T1 cells and (C) MDA-MB-231 cells treated with various concentrations of OTAB NPs and OTAB@cRGD NPs with or without 808 nm laser irradiation (1.0 W cm^{-2}). (D) Fluorescence images of live (green)/dead (red) 4T1 cells loaded with calcein-AM and PI. Scale bars: 100 μm. (E) NIR-II imaging of 4T1 cells after incubating with OTAB NPs and OTAB@cRGD NPs at different time points (808 nm, 0.3 W cm^{-2}). (F) Relative fluorescence intensity of each graph in panel (E). (G) CLSM images of intracellular fluorescence intensities of MDA-MB-231 cells incubated with OTAB NPs and OTAB@cRGD NPs for different time periods (808 nm, 1.0 W cm^{-2}). The fluorescence images were collected at 600–650 nm (λ_{ex}: 559 nm). Scale bars: 25 μm. (H) Relative fluorescence intensity of each graph in panel (G). (I) CLSM images for MDA-MB-231 cells after treatment with OTAB@cRGD NPs loaded with DCFH-DA under hypoxic and normoxic conditions (808 nm, 1.0 W cm^{-2}). Scale bars: 25 μm. All statistical data are represented as mean ± SD ($n = 3$; *$P < 0.05$, **$P < 0.01$, and ***$P < 0.001$).

indicating that OTAB NPs and OTAB@cRGD NPs were biocompatible in the dark. In contrast, the OTAB@cRGD NPs group showed a significant increase in dead cells after irradiation with an 808 nm laser (1.0 W cm^{-2}) for 5 min. Stronger red fluorescence was observed in 4T1 cells in the OTAB@cRGD NPs group compared to the irradiated OTAB NPs group, suggesting that OTAB@cRGD NPs could kill the cells more completely due to the cRGD targeting properties. The above results showed that OTAB@cRGD NPs had good anti-tumor cell ability *via* PDT and PTT, which eventually induced apoptosis.

To further verify the targeting effect of the NPs, OTAB@cRGD NPs and OTAB NPs were incubated with 4T1 cells and analyzed by using an NIR-II imaging system. Fig. 3E showed that fluorescence signals continuously increased with the prolongation of incubation time. The fluorescence intensity of the targeted nanoparticle group was 1.37 times higher than that of the non-targeted nanoparticle group after incubation for 10 h (Fig. 3F). This proved that OTAB@cRGD NPs had an excellent targeting effect on tumor cells. Since the emission wavelength of nanoparticles is greater than 1000 nm, the same mass of Nile Red (NR) was then wrapped into nanoparticles in order to observe the cellular NPs using confocal laser scanning microscopy (CLSM). Particle size maps and absorption spectra demonstrated that Nile red hybrid nanoparticles have been successfully prepared (Fig. S25†). The red fluorescence of cells after incubation with OTAB@cRGD-NR NPs was stronger than that with OTAB-NR NPs under the same conditions (Fig. 3G and H), which further verified the targeting effect of cRGD-modified NPs.

In order to investigate whether the ROS-generating ability of OTAB@cRGD NPs was oxygen-dependent or oxygen-independent, we performed the cellular ROS production experiments under normoxic and hypoxic conditions. The fluorescence intensity of MDA-MB-231 cells treated with non-laser-irradiated OTAB@cRGD NPs was negligible, suggesting that OTAB@cRGD NPs were unable to produce ROS in the dark. In contrast, after laser irradiation treatment, green fluorescence was observed in MDA-MB-231 cells under both normoxic and hypoxic conditions, which was attributed to the oxidation of non-fluorescent DCFH-DA probe to highly fluorescent DCF by ROS (Fig. 3I). Thus, these results confirmed that the OTAB@cRGD NPs can produce ROS *via* a type-I pathway, presenting oxygen-independent PDT for superior anti-tumor treatment.

NIR-II guided anticancer therapy of OTAB@cRGD NPs *in vivo*

Prior to seeking *in vivo* tumor diagnosis and treatment, we performed a biosafety assessment of OTAB@cRGD NPs and OTAB NPs. Nanoparticles were injected intravenously into BALB/c female mice. No significant changes in the body weight of the mice were observed within 20 days (Fig. 4A). At 20 days after injection, the major organs were collected for *in vivo* biosafety evaluation. As shown in Fig. 4B, there were no obvious abnormalities observed in the H&E staining of major organ

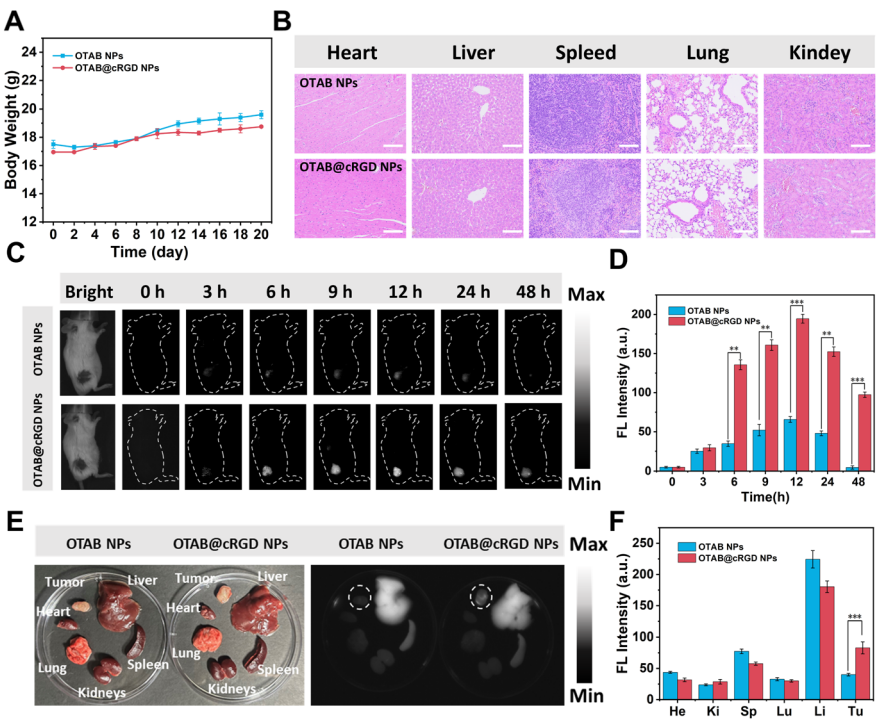

Fig. 4 (A) The weight change curves of normal mice after intravenous injection of OTAB NPs and OTAB@cRGD NPs. (B) H&E staining of the main organs extracted from the mice in the various groups at the end of the treatments. Scale bars: 100 μm. (C) Real-time fluorescence images of 4T1 tumor-bearing mice for OTAB NPs and OTAB@cRGD NPs signals at 0, 3, 6, 9, 12, 24, and 48 h post-injection (808 nm, 0.3 W cm^{-2}). (D) The corresponding FL intensity curve of tumors. (E) Fluorescence images of major organs and tumor tissues at 48 h post-injection. (F) The corresponding fluorescence intensities of excised tumors and major organs. All statistical data are represented as mean ± SD ($n = 3$; $^{**}P < 0.01$, and $^{***}P < 0.001$).

tissues in the nanoparticle-injected mice. These results indicated that the nanoparticles have good biocompatibility *in vivo*.

Inspired by its impressive NIR-II emission and *in vitro* phototherapeutic performance, further *in vivo* imaging of the 4T1 tumor was evaluated. To investigate the biodistribution of OTAB NPs and OTAB@cRGD NPs, 4T1 tumor-bearing BALB/c mice were selected for NIR-II imaging monitoring at different times (0, 3, 6, 9, 12, 24 and 48 h). When the tumor grew to ≈100 mm^3, OTAB@cRGD NPs and OTAB NPs were injected *via* the tail vein of the mice to capture NIR-II images of the tumor (808 nm, 0.3 W cm^{-2}). As shown in Fig. 4C and D, the accumulation of OTAB NPs at the tumor site was insufficient. However, the fluorescence intensity of the OTAB@cRGD NPs tumor site gradually increased and reached a peak at 12 h, followed by a gradual decrease in fluorescence intensity. Then 12 h was selected as the optimal treatment time for subsequent phototherapy. OTAB@cRGD NPs preferentially accumulated in the tumor site due to the tumor-targeting effect of cRGD. At 48 h post-injection, the mice were executed, and major organs and tumors were taken for imaging and analysis. Fig. 4E and F showed that the nanoparticles readily accumulated in the liver and spleen, suggesting that OTAB@cRGD NPs and OTAB NPs were metabolized predominantly by the liver. Compared with OTAB NPs, OTAB@cRGD NPs were more inclined to accumulate at the tumor site, which showed that OTAB@cRGD NPs containing cRGD had good NIR-II tumor imaging properties, enabling subsequent PDT/PTT synergistic therapy. Then, 4T1 tumor-bearing BALB/c mice were divided into six groups randomly and injected with PBS, OTAB NPs and OTAB@cRGD NPs *via* the tail vein, respectively (Fig. 5A). At 12 h after injection, the irradiated groups received 808 nm laser irradiation (0.8 W cm^{-2}). The *in vivo* photothermal imaging showed that the tumor temperature of the OTAB@cRGD NPs-treated mice increased by 18.7 °C under 808 nm laser irradiation due to

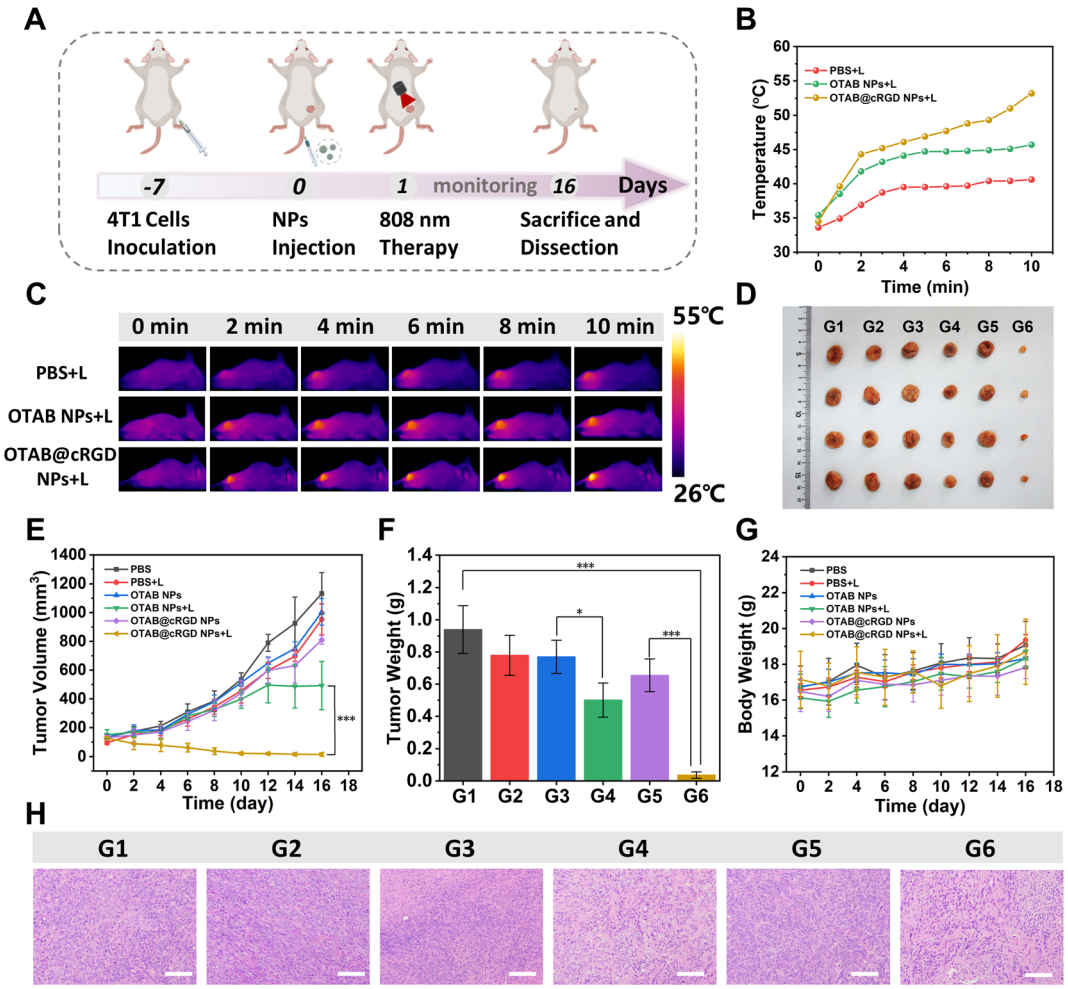

Fig. 5 (A) The schematic diagram of 4T1 tumor-bearing mouse model building and treatment *in vivo*. (B) Tumor temperatures of mice monitored by the IR thermal camera as a function of the irradiation time. (C) IR thermal graphs of 4T1 tumor-bearing mice after the intravenous injection with PBS, OTAB NPs and OTAB@cRGD NPs for 12 h and then treated with 808 nm laser irradiation (0.8 W cm^{-2}). (D) Representative photographs of the tumors extracted from the mice in the various groups at the end of the treatments. (E) Relative tumor volume growth curves of the mice in different groups. (F) Tumor weights of the different treated groups. (G) The body weight curves of mice in different groups during the process of therapy. (H) H&E staining images of tumors. Scale bar: 100 μm. G1: PBS; G2: PBS + L; G3: OTAB NPs; G4: OTAB NPs + L; G5: OTAB@cRGD NPs; G6: OTAB@cRGD NPs + L. All statistical data are represented as mean ± SD ($n = 3$; *$P < 0.05$ and ***$P < 0.001$).

OTAB@cRGD NPs selectively accumulating in the tumor region (Fig. 5B and C), confirming the excellent photothermal performance of OTAB@cRGD NPs *in vivo*. However, the tumor temperature of the OTAB NPs treatment group was only elevated by approximately 10.3 °C due to the OTAB NPs' lack of active targeting ability, whereas no significant temperature elevation was observed in the PBS-treated group. Subsequently, the *in vivo* phototherapeutic effects of OTAB@cRGD NPs or OTAB NPs were further evaluated in 4T1 tumor-bearing BALB/c mice. Tumor volume and body weight were monitored every two days to estimate the treatment outcome during the treatment period. The results of tumor photographs (Fig. 5D), tumor volumes (Fig. 5E) and tumor weights (Fig. 5F) showed that tumors in PBS, OTAB NPs and OTAB@cRGD NPs groups increased rapidly without laser irradiation, with little or no anti-tumor effect. Under 808 nm laser irradiation, the tumor inhibition rate of OTAB NPs was 56.6 ± 18.3%, which is attributed to the EPR effect of the nanoparticles. Encouragingly, at 16 days after inoculation, the tumor volume of the OTAB@cRGD NPs treated mice was significantly smaller than that of the control mouse groups. The tumor inhibition rate of OTAB@cRGD NPs was 87.9 ± 7.8% due to the efficient PDT/PTT synergistic therapy, which further showed the outstanding type-I PDT/PTT synergistic therapeutic efficacy in defeating tumors. The mice photographs (Fig. S26†), body weights (Fig. 5G), and organ photographs (Fig. S27†) showed that the nanoparticles were not significantly toxic. No obvious tissue damage was observed from the H&E staining of the internal organs collected after treatment in Fig. S28†. As shown in Fig. 5H, H&E staining of the tumor showed obvious tissue damage in the "OTAB@cRGD NPs + L" group compared with other groups. These results indicated that OTAB@cRGD NPs can achieve efficient NIR-II imaging-guided type-I PDT/PTT therapeutic efficacy without significant toxicity.

Conclusions

In summary, we successfully designed and synthesized a novel NIR-II aza-BODIPY-based phototheranostics system, which combined NIR-II imaging and type-I PDT and PTT properties by regulating the band gap. By virtue of the strategy of D–A–D, the emission peak of OTAB successfully reached the NIR-II region. After forming OTAB@cRGD NPs by self-assembly with DSPE-PEG_{2000}-cRGD, a single 808 nm laser can trigger integrated NIR-II imaging diagnosis and treatment. The nanoparticles showed excellent $O_2^{\bullet-}$ generation ability, enabling type-I PDT. Also, good photothermal conversion efficiency was obtained from the OTAB@cRGD NPs. *In vitro* and *in vivo* experiments showed that OTAB@cRGD NPs could serve as an all-in-one phototheranostic agent for NIR-II imaging-guided synergistic type-I PDT/PTT therapy. Overall, we believe that this strategy provides valuable insights for the design of phototheranostics and integration of NIR-II diagnosis and treatment.

Ethical statement and animal model

All animal procedures were performed in accordance with the Guidelines for Care and Use of Laboratory Animals of Shaanxi Normal University and approved by the Animal Ethics Committee of Shaanxi Normal University (20230207-1). BALB/c mice (female, 4–5 weeks, 15–20 g) were purchased from the Experimental Animal Center of Shaanxi Normal University. The right posterior region of the BALB/c mice was injected with 1×10^6 4T1 cells *via* subcutaneous injection to obtain a 4T1 tumor-bearing mice model.

Data availability

All relevant data have been included in the main text and the ESI.†

Author contributions

Y. X. R. and Y. L. T. conceived the project. Y. X. R., L. L. and X. Y. Z. contributed to the synthesis, characterization and data analysis. Y. X. R., Q. Y., B. K. B. and M. Q. L. contributed to the acquisition of partial data. Y. X. R. wrote the original draft. Y. L. T. supervised the project. Y. L. T. validated, reviewed and edited the writing. All authors have given approval to the final version of the manuscript.

Conflicts of interest

There are no conflicts to declare.

Acknowledgements

This work was financially supported by the National Natural Science Foundation of China (Grant No. 22274095 and 21974084), and the Fundamental Research Funds for the Central Universities (GK202302004). The authors thank Xin-Ai Guo (School of Chemistry and Chemical Engineering, Shaanxi Normal University) for her kind support in using the Infrared region II *in vivo* imaging system.

Notes and references

1 V. Shanmugam, S. Selvakumar and C.-S. Yeh, *Chem. Soc. Rev.*, 2014, **43**, 6254–6287.
2 Z. Zhang, Y. Zhou, S. Zhao, L. Ding, B. Chen and Y. Chen, *Adv. Sci.*, 2022, **9**, 2203583.
3 K. Wei, Y. Wu, X. Zheng, L. Ouyang, G. Ma, C. Ji and M. Yin, *Angew. Chem., Int. Ed.*, 2024, **63**, e202404395.
4 S.-B. Wang, C. Zhang, J.-J. Ye, M.-Z. Zou, C.-J. Liu and X.-Z. Zhang, *ACS Cent. Sci.*, 2020, **6**, 555–565.
5 S. Li, K. Gu, H. Wang, B. Xu, H. Li, X. Shi, Z. Huang and H. Liu, *J. Am. Chem. Soc.*, 2020, **142**, 5649–5656.
6 P. Wu, Y. Zhu, S. Liu and H. Xiong, *ACS Cent. Sci.*, 2021, **7**, 2039–2048.
7 J. Huang and K. Pu, *Angew. Chem., Int. Ed.*, 2020, **59**, 11717–11731.
8 C. Wang, L. Zhou, C. Liu, J. Qiao, X. Han, L. Wang, Y. Liu, B. Xu, Q. Qiu, Z. Zhang, J. Wang, X. Zhou, M. Zeng, L. Yu and L. Fu, *Nat. Commun.*, 2024, **15**, 6362.

9 W. Zhang, M. Kang, X. Li, H. Yang, Z. Zhang, Z. Li, Y. Zhang, M. Fan, C. Liao, C. Liu, G. Xu, D. Wang, Z. Xu and B. Z. Tang, *Adv. Mater.*, 2024, **36**, 2406474.
10 G. Qi, K. Chen, W. Guan, J. Xie, X. Chen, G. Zhang, R. Yan and G. Yang, *ACS Appl. Mater. Interfaces*, 2024, **16**, 49083–49091.
11 K.-X. Teng, L.-Y. Niu, Y.-F. Kang and Q.-Z. Yang, *Chem. Sci.*, 2020, **11**, 9703–9711.
12 M. Zhu, H. Zhang, G. Ran, D. N. Mangel, Y. Yao, R. Zhang, J. Tan, W. Zhang, J. Song, J. L. Sessler and J.-L. Zhang, *J. Am. Chem. Soc.*, 2021, **143**, 7541–7552.
13 G. Jia, Q. Wu, M. Hou, Y. Jiang, H. Yang, M. Li, X. Wu and C. Zhang, *Adv. Healthcare Mater.*, 2024, **13**, 2402079.
14 C. Li, J. Ye, X. Yang, S. Liu, Z. Zhang, J. Wang, K. Zhang, J. Xu, Y. Fu and P. Yang, *ACS Nano*, 2022, **16**, 18143–18156.
15 W. Qiao, T. Ma, G. Xie, J. Xu, Z.-R. Yang, C. Zhong, H. Jiang, J. Xia, L. Zhang, J. Zhu and Z. Li, *ACS Nano*, 2024, **18**, 25671–25684.
16 Z.-S. Yang, Y. Yao, A. C. Sedgwick, C. Li, Y. Xia, Y. Wang, L. Kang, H. Su, B.-W. Wang, S. Gao, J. L. Sessler and J.-L. Zhang, *Chem. Sci.*, 2020, **11**, 8204–8213.
17 D. Liu, Y. Li, H. Zhang, B. Wang, C. Yao, M. Lan, Z. Yang and X. Song, *Chin. Chem. Lett.*, 2025, **36**, 109910.
18 H. Zhao, Y. Wang, Q. Chen, Y. Liu, Y. Gao, K. Müllen, S. Li and A. Narita, *Adv. Sci.*, 2024, **11**, 2309131.
19 L. Bai, P. Sun, Y. Liu, H. Zhang, W. Hu, W. Zhang, Z. Liu, Q. Fan, L. Li and W. Huang, *Chem. Commun.*, 2019, **55**, 10920.
20 J. Wang, C. Yu, E. Hao and L. Jiao, *Coord. Chem. Rev.*, 2022, **470**, 214709.
21 X. Guo, J. Yang, M. Li, F. Zhang, W. Bu, H. Li, Q. Wu, D. Yin, L. Jiao and E. Hao, *Angew. Chem., Int. Ed.*, 2022, **61**, e202211081.
22 Y.-C. Liu, G.-J. Liu, W. Zhou, G.-L. Feng, Q.-Y. Ma, Y. Zhang and G.-W. Xing, *Angew. Chem., Int. Ed.*, 2023, **62**, e20230978.
23 T. Xiong, M. Li, Y. Chen, J. Du, J. Fan and X. Peng, *Chem. Sci.*, 2021, **12**, 2515–2520.
24 K. Wen, H. Tan, Q. Peng, H. Chen, H. Ma, L. Wang, A. Peng, Q. Shi, X. Cai and H. Huang, *Adv. Mater.*, 2022, **34**, 2108146.
25 Z. Wang, C. Li, S. Huang, X. Ma, Y. Sun, J. Zhao and S. Gou, *Mater. Today Nano*, 2022, **18**, 100220.
26 L. Fang, R. Huang, W. Gong, Y. Ji, Y. Sun, S. Gou and J. Zhao, *Small*, 2024, **20**, 2307414.
27 K.-X. Teng, L.-Y. Niu and Q.-Z. Yang, *J. Am. Chem. Soc.*, 2023, **145**, 4081–4087.
28 J. Zhao, R. Huang, Y. Gao, J. Xu, Y. Sun, J. Bao, L. Fang and S. Gou, *ACS Mater. Lett.*, 2023, **5**, 1752–1759.
29 B. Wang, H. Zhou, L. Chen, Y. Ding, X. Zhang, H. Chen, H. Liu, P. Li, Y. Chen, C. Yin and Q. Fan, *Angew. Chem., Int. Ed.*, 2024, **63**, e202408874.
30 Y. Wang, Y. Li, Z. Zhang, L. Wang, D. Wang and B. Z. Tang, *Adv. Mater.*, 2021, **33**, 2103748.
31 H. Wen, Z. Zhang, M. Kang, H. Li, W. Xu, H. Guo, Y. Li, Y. Tan, Z. Wen, Q. Wu, J. Huang, L. Xi, K. Li, L. Wang, D. Wang and B. Z. Tang, *Biomaterials*, 2021, **274**, 120892.
32 L. Fang, Q. Meng, Y. Zhang, R. Su, F. Xing, H. Yang, Y. Hou, P. A. Ma, K. Huang and S. Feng, *ACS Nano*, 2023, **17**, 21553–21566.
33 J. Killoran, L. Allen, J. F. Gallagher, W. M. Gallagher and D. F. O'Shea, *Chem. Commun.*, 2002, 1862–1863.
34 Y. Li, D. Zhang, Y. Yu, L. Zhang, L. Li, L. Shi, G. Feng and B. Z. Tang, *ACS Nano*, 2023, **17**, 16993–17003.
35 H. Bian, D. Ma, X. Zhang, K. Xin, Y. Yang, X. Peng and Y. Xiao, *Small*, 2021, **17**, 2100398.
36 H. Pan, S. Li, J.-l. Kan, L. Gong, C. Lin, W. Liu, D. Qi, K. Wang, X. Yan and J. Jiang, *Chem. Sci.*, 2019, **10**, 8246–8252.
37 Y. Tian, H. Zhou, Q. Cheng, H. Dang, H. Qian, C. Teng, K. Xie and L. Yan, *J. Mater. Chem. B*, 2022, **10**, 707–716.
38 L. Li, X. Zhang, Y. Ren, Q. Yuan, Y. Wang, B. Bao, M. Li and Y. Tang, *J. Am. Chem. Soc.*, 2024, **146**, 5927–5939.
39 D. Li, X. Chen, D. Wang, H. Wu, H. Wen, L. Wang, Q. Jin, D. Wang, J. Ji and B. Z. Tang, *Biomaterials*, 2022, **283**, 121476.